SAND2016-4636J

Aerosol Utilization Efficiency in Particulate Injection Inductively Coupled Plasma Mass Spectrometry

Joshua A. Hubbard and Joseph A. Zigmond

Sandia National Laboratories

Albuquerque, New Mexico

Corresponding Author: Josh Hubbard, 505-844-0879, jahubba@sandia.gov

Abstract

An electrostatic size classification technique was used to segregate particles of known composition prior to being injected into an inductively coupled plasma mass spectrometer (ICP-MS). Size segregated particles were counted with a condensation nuclei counter as well as sampled with an ICP-MS. By injecting particles of known size, composition, and aerosol concentration into the ICP-MS, order of magnitude aerosol utilization efficiencies were calculated and the particle size dependencies for volatile and refractory species were quantified. Aerosol utilization efficiency was defined as the rate at which atoms were detected in the ICP-MS normalized by the rate at which atoms were injected in the form of particles. This method adds valuable insight into the development of technologies like laser ablation ICP-MS where aerosol particles (mostly of unknown size and gas concentration) are generated during ablation and then transported into the plasma of an ICP-MS. In this study, we characterized aerosol utilization efficiencies of volatile species gold and silver along with refractory species aluminum oxide, cerium oxide, and yttrium oxide. Aerosols were generated with electrical mobility diameters ranging from 100 nanometers (nm) to 1000 nm. In general, it was observed that refractory species had lower aerosol utilization efficiencies than volatile species and there were strong dependencies on particle size and plasma torch residence time. Volatile species showed a distinct transition point at which aerosol utilization efficiency began decreasing with increasing particle size. This critical diameter indicated the largest particle size for which complete particle utilization should be expected and agreed with theories published in other works. Aerosol utilization efficiencies also displayed power law dependencies with respect to particle size. Particle composition and plasma residence time affected these power law dependencies. Aerosol utilization efficiencies ranged from 10^{-5} to 10^{-11}, which may be low due to the use of a nitrogen/argon dilution technique needed to perform simultaneous aerosol and ICP-MS measurements. Free molecular heat and mass transfer theory was applied to predict experimentally observed behavior. Evaporative phenomena were not sufficient to explain the dependence of aerosol utilization on particle size. We hypothesize that boiling phenomena may be responsible for augmented heat and mass transfer rates. Additional work is needed to

correlate experimental data with theory for oxidized species where thermodynamic property data is sparse relative to pure elements.

1 Introduction

Aerosol particles are generated during laser ablation of solid surfaces through processes like vapor condensation. Laser Ablation Inductively Coupled Plasma Mass Spectrometry (LA-ICP-MS) technologies are designed to generate particles, and then aspirate them into an ICP-MS, thereby characterizing solid surfaces without sample digestion and wet chemistry. Spatial inhomogeneity of solid samples can also be characterized and material characterization can be performed more rapidly using LA-ICP-MS. Although promising, sample fractionation (preferential sampling and detection of certain elements) can occur and is difficult to mitigate without matrix-matched certified reference materials. Complex thermal processes and aerosol transport make it difficult to know actual characteristics, i.e., particle size distribution and composition, of the aerosol aspirated by the ICP-MS without direct measurement. Similar thermal and transport processes then govern sample utilization and detection efficiencies in ICP-MS by affecting the breakdown of aerosol particles into constituent atoms. The objective of this study was to generate aerosols of known size, aerosol concentration, and composition, and benchmark the performance of an ICP-MS instrument for direct injection of particulate. This approach separates the process of aerosol generation via laser ablation from complex particle-plasma interactions occurring inside the ICP-MS thereby enabling better characterization of the latter processes. This data can also be used to optimize laser ablation systems (e.g., wavelength) such that LA-ICP-MS technologies are more sensitive and robust for complex samples.

This study focuses on thermal processes inside the inductively coupled plasma. For this reason, a few basic characteristics of the ICP environment lend to better understanding of aerosol-plasma interactions. Hanselman et al. (1994) reference temperatures of approximately 7000 K inside the plasma where ion densities are approximately 10^{15} ions/cm^3. Local thermodynamic equilibrium is often assumed in both experimental and computational studies. Tendero et al. (2006) define local-thermal-equilibrium (LTE) as the condition at which the electron temperature equals the gas temperature. Electron energy is consumed by collisions with heavy gas atoms in LTE. Tendero et al. also define non-local-thermal-equilibrium (non-LTE) as the occurrence of elastic collisions between gas atoms and plasma electrons. Non-LTE conditions can occur due to the presence of interferents and other conditions leading to local gas temperatures as much as 2000 K less than the local electron temperatures. In practice, non-LTE conditions are often assumed for low pressure plasmas and LTE conditions assumed for atmospheric pressure plasmas which are the focus of this work. In actuality both non-LTE and LTE conditions occur inside an ICP torch where the central core more closely approximates LTE conditions and the peripheral does not. ICP modeling capabilities of electron density, electron temperature, and gas temperature are within 10-20% of experimentally observed values (Yang et al. 2000). Punjabi et al (2014) applied the Saha equation to show that less than about 0.1% of

Argon gas is ionized in an ICP and we can therefore treat the plasma as a hot gas to good approximation.

1.1 Particle-plasma interactions

A number of formative studies were conducted regarding heat and mass transfer to aerosol particles inside plasmas where the particle sizes typically ranged from 10-100 μm in particle diameter: Chen and Pfender (1982a, 1982b, 1983a, 1983b), Lee et al. (1985), Pfender (1985), Pfender and Lee (1985), Young and Pfender (1985,1987), Lee and Pfender (1987), and Chen (1988). In these studies, the authors found that continuum heat and mass transfer correlations needed to be corrected for non-continuum effects inside the plasma. More recently, a number of studies have characterized aerosol processing inside plasmas. Bernardi et al. (2004) modeled the particle-plasma coupling with evaporation in the commercially available software tool ANSYS Fluent. Bernardi et al. (2004) did not model conduction heat transfer within the particle and assumed that the particle reaches its melting point, the liquid phase fraction increases, and then the particle increases in temperature once it has completely melted giving rise to evaporative mass transfer. Lindner and Bogaerts (2011) modeled aerosol processing in ICP and showed higher gas temperatures were possible when helium was used as the injection medium thus resulting in larger droplets more completely evaporating. Flamingi et al. (2012) also studied the vaporization of aerosol particles in ICP-OES and ICP-MS and noted a difference in analyte detection for pure metals and metal-oxides.

1.2 LA-ICP-MS

LA-ICP-MS is simply, or not so simply, coupling a laser ablation cell onto the front end of an ICP-MS to analyze solid samples directly by creating aerosols during laser ablation. Complex aerosol generation processes have been characterized for metal and glass solid samples (Gonzalez et al. 2007a, 2007b). LA-ICP-MS has been shown to produce detection efficiencies on the order of 10^{-8} to 10^{-5} for silicate glasses, zircon, and silicon, where the addition of helium as a carrier gas enhanced detection efficiencies by as much as a factor of five with respect to particles transported in Argon (Walle et al. 2009). Glaus et al. (2010) showed that enhancements to LA-ICP-MS were achieved by moving from infrared laser wavelengths to deep ultraviolet wavelengths and reducing laser pulse durations from nanoseconds to femtoseconds. These two modifications in laser characteristics lead to narrower particle size distributions with smaller mean particle diameters. They also found that micrometer sized particles could be present in the post-ablation gas through the coalescence of 10 nanometer primary particles. Koch et al. (2010) were able to measure these micrometer sized particles with an optical counter. Kovacs et al. (2010) have also employed helium as carrier gas to enhance the transport efficiency of particles from the surface being ablated. They attributed better performance to higher gas thermal conductivity and its influence on aerosol expansion, more efficient vapor transport away from surface, and desirable effects on plasma operation.

1.3 Aerosol conditioning

Gas exchange has been used in several studies to augment the performance of analytical instruments. Typically aerosol measurement instruments operate optimally with air and nitrogen gases. The converse is true for ICP-MS. The addition of air or nitrogen to the plasma flow typically makes the plasma unstable and unusable for analytical purposes. The use of argon in electrostatic aerosol instruments can affect electrical breakdown strengths and aerodynamic particle behavior due to differences in gas density and viscosity. Okada et al. (2002) employed argon gas inside a differential mobility analyzer to size classify particles in the 5-40 nm size range which were subsequently injected into an ICP-MS. Nishiguchi et al. (2008) used a gas converter apparatus consisting of concentric tubes to exchange nitrogen for argon; the inner tube was porous and permitted the diffusional exchange of gas ions but did not permit the loss of particles. Kovacs et al. (2010) also used a gas exchange device to replace air with argon before particle injection into the ICP-MS thereby enhancing ICP-MS performance. Myojo et al. (2010) used a similar approach, exchanging air for argon, but used the sheath and aerosol flows inside a Kanawa-type differential mobility analyzer to dilute the air with argon.

2 Experiment

Aerosols of known composition were generated in ultra-high purity nitrogen. The test apparatus is shown in Figure 1. For good measure, the nitrogen was passed through carbon and HEPA capsule filters to ensure that no volatile gases or particulates were present. The nitrogen flow was regulated by a mass flow controller (Alicat MCRW), passed through an in-line bipolar gas ionizer (Simco-Ion Ioncell), and fed into an aerosol generation chamber constructed from a stainless steel tube 0.46 meters (m) in length (18 inches, in) and 0.2 m (8 in) in diameter with two end flanges. A 180 kHz ultrasonic spray nozzle (Sonotek) was inserted into the top flange with an ISO-KF bulkhead fitting so the spray went directly into the chamber. The aerosol generation chamber was wrapped in a blanket heater (Briskheat 12 in x 24 in) which was controlled by an Omega temperature controller (CSI8DH). A T-type thermocouple was used to measure the gas temperature inside the chamber. The temperature was maintained at 43.3°C (110°F) to enhance droplet evaporation for low gas flows. Psychrometric calculations were performed to ensure that the nitrogen could carry the amount of moisture injected into the chamber with the ultrasonic nozzle.

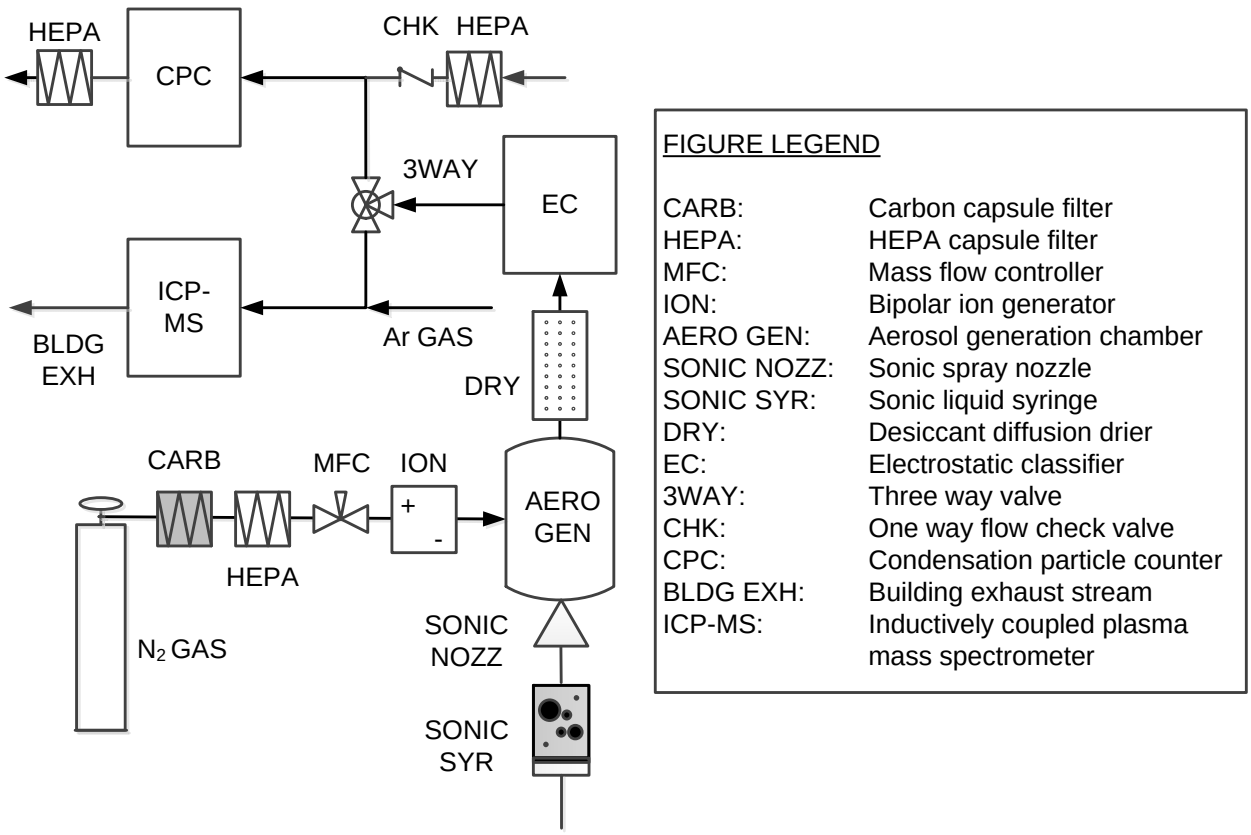

Figure 1. Experimental test apparatus used to generate aerosols of known size and composition, measure the aerosol gas concentration, and inject the aerosol directly into an ICP-MS

Test powders were placed in 50 mL centrifuge tubes, mixed with water, sonicated, and then drawn into a sonic syringe (Sonotek) capable of keeping heavy particles suspended over many hours of testing. A syringe pump (Cole Parmer) was used to deliver a constant rate of 25 µL/min of colloid solution to the Sonotek Nozzle. The aerosol was then passed through two desiccant diffusion driers (Topas DDU-570) to remove water vapor from the aerosol stream. From there, the dry aerosol was fed into an electrostatic classifier (TSI 3080 with 3088 advanced aerosol neutralizer and 3081 long DMA) to size segregate the particles. Size segregated particles were then either fed into either (1) a condensation particle counter (TSI Inc. 3787) to measure particle concentration (#/cm^3 of N_2), or (2) into a Perkin-Elmer Elan DRC II Inductively Coupled Plasma Mass Spectrometer. The ICP-MS injector was modified to accommodate its connection to 6 millimeter (0.25 in) tubing. Initial attempts were made to operate the electrostatic classifier and condensation particle counter with argon. These attempts were not successful and for this reason we generated aerosols into nitrogen with flow rates ranging from 0.1-0.25 liters per minute. After electrostatic size segregation the aerosol stream was mixed with argon gas flowing at rates between 1.0-1.5 liters per minute (lpm). High argon flow rates were needed to keep the argon plasma stable with the presence of nitrogen. The introduction of nitrogen was an off-normal operating condition for the ICP-MS but necessary to perform measurements with the

electrostatic classifier and condensation particle counter. In the future we plan to compare the efficacy of this approach (generating aerosol into N_2 and then mixing with argon) with the efficacy of using a N_2-Ar gas exchanger and helium co-injection.

Two nitrogen flows were used during experiments, 0.1 lpm (low flow) and 0.25 lpm (high flow). The electrostatic classifier sheath:aerosol flow rate ratios for the low and high flow conditions were 10:1 and 7.2:1, respectively. Low sheath flow rates were required to extend the working range of the classifier up to 1000 nanometers in electrical mobility diameter. At low sheath:aerosol flow rate ratios (< 5:1), the performance of the classifier is less optimal and the size classification is more broad than at a ratio of 10:1 (Flagan 2008). The aerosol flow rate of the condensation particle counter was adjusted to the low and high flow settings of 0.1 and 0.25 lpm using a DryCal gas flow calibrator (Mesa Labs). The two instruments, classifier and CPC, were operated as a scanning mobility particle sizer (SMPS) where the classifier voltage was ramped over time to give measurements of aerosol concentration from 100-1000 nanometers in electrical mobility diameter over a time period of 300 seconds. When classified and injected directly into the ICP-MS, the same 300 second ramp was used to deliver a stream of size segregated particles to the ICP-MS over time. Thus, the instantaneous sample time for each ICP-MS measurement was directly correlated to particle size.

ICP-MS flows were as follows: (1) argon nebulizer flow (premixed with the aerosol) of 1.5 lpm for the high flow condition and 1.0 lpm for the low flow condition, (2) argon auxiliary flow of 1.2 lpm, and (3) argon plasma flow of 15 lpm. The torch power was kept constant at 1400 Watts. Argon nebulizer flows in excess of 0.5 lpm may not be common in many ICP-MS measurements since this reduces the residence time inside the plasma and may affect the inner plasma core structure. However, the introduction of nitrogen into the plasma quenched the torch unless these high argon flow rates were used to stabilize the plasma. We hypothesize that the addition of helium to the aerosol flow may stabilize the plasma at lower Ar:N_2 flow rate ratios and allow for increased particle residence time inside the torch.

The ICP-MS software was used to setup methods for each of the materials analyzed. Along with the analyte of interest, all of its potential oxidation states and isotopes (e.g., ^{107}Ag and ^{109}Ag) were monitored. The argon dimer and water were also used as monitors for the performance of the ICP-MS. When switching from one material to the next, e.g., Ag to Au, the aerosol generation chamber was purged with argon at a rate of 10 lpm for 8-12 hours to ensure that no aerosol particles were carried over from one experiment to the next. In addition to the oxide forms of the analyte of interest, the previous analyte of interest (last test material) was monitored to ensure there was no residual aerosol in the test system. Settings for the aerosol instruments and ICP-MS instrument are given below for the high and low flow test conditions.

Table 1. Aerosol and ICP-MS instrument settings for the high and low flow test conditions

		Test Condition	
Instrument setting	**unit**	**High N_2 flow**	**Low N_2 flow**
EC sheath flow	(lpm)	1.8	1
EC aerosol flow	(lpm)	0.25	0.1
Sheath:Aerosol flow ratio	(-)	7.2	10
ICP-MS Ar nebulizer flow	(lpm)	1.5	1
ICP-MS Ar auxiliary flow	(lpm)	1.2	1.2
ICP-MS Ar plasma flow	(lpm)	15	15
ICP-MS Ar torch power	(W)	1400	1400

Five powders were selected to represent a range of volatile to refractory behavior inside the plasma: silver (Ag), gold (Au), aluminum oxide (Al_2O_3), cerium oxide (CeO_2), and yttrium oxide (Y_2O_3). The supplier and model for each powder are given in Table 2 along with the minimum and maximum physical particle sizes provided by the manufacturer. For each material, molecular weight (MW), material density (ρ_m), melting point temperature (T_{mp}), boiling point temperature (T_{bp}), specific heat capacity (C_p), and thermal diffusivity (α) are given below in Table 3. Silver and gold have relatively low melting points and thermal heat capacities with respect to the oxidized species. We hypothesized that the total aerosol utilization efficiency would be higher for these two materials and lower for the oxidized species.

Table 2. List of powders, manufacturer information, and manufacturer specified minimum and maximum physical particle sizes

Name	**Symbol**	**Supplier**	**Purity**	**Model**	**Min. size**	**Max. size**
(-)	**(-)**	**(-)**	**(%)**	**(-)**	**(µm)**	**(µm)**
Silver	Ag	Advanced Materials	99.95	47MR-01C	0.1	0.5
Aluminum Oxide	Al_2O_3	Skyspring	99.99	1321DL	0.3	0.8
Gold	Au	Alfa Aesar	99.96	44636	0.5	0.8
Cerium Oxide	CeO_2	Skyspring	99.9	2113CG	0.1	1.0
Yttrium Oxide	Y_2O_3	Skyspring	99.995	8211CG	0.5	1.0

Table 3. Molecular weight (MW), material density (ρ_m), melting point temperature (T_{mp}), boiling point temperature (T_{bp}), specific heat capacity (C_p), thermal conductivity (k) and thermal diffusivity (α) for test materials.

Name	MW	ρ_m	T_{mp}	T_{bp}	C_p	k	α
(-)	(g/mol)	(g/cm^3)	(°C)	(°C)	(J/g·K)	(W/mK)	(m^2/s)
Silver	107.87	10.49	962	2162	0.24	406	1.6E-04
Aluminum Oxide	101.96	3.95	2072	2977	0.88	20	5.8E-06
Gold	196.96	19.32	1064	2970	0.13	314	1.3E-04
Cerium Oxide	172.12	7.65	2400	3500	0.45	11	3.1E-06
Yttrium Oxide	225.81	5.1	2425	4300	0.45	27	1.2E-05

Scanning electron microscope images were also taken for each of the powders. For the SEM samples to be most representative of the aerosolized materials, the colloidal suspension sprayed into the chamber was first sonicated in a 50 mL centrifuge tube. A small drop of each solution was then placed on a separate electron microscopy stub for imaging. SEM images are shown in Figure 2. In this study we will assume that the electrical mobility diameter is a good proxy for true physical diameter since the particles are roughly spherical (DeCarlo et al. 2004). Additional measurement techniques would be required to obtain true shape factors but SEM images do not reveal particle morphologies substantially different from spherical (e.g., platelets). In this study we suspended test powders in water and then atomized the liquid to create aerosols. By spraying dilute solutions we attempted to mitigate the occurrence of agglomerated particles. To confirm our assumption of non-agglomerated particles, true particle density measurements (McMurry et al. 2002; Lee et al. 2009) could be made with proper instrumentation. However, instrumentation required for these measurements was not available.

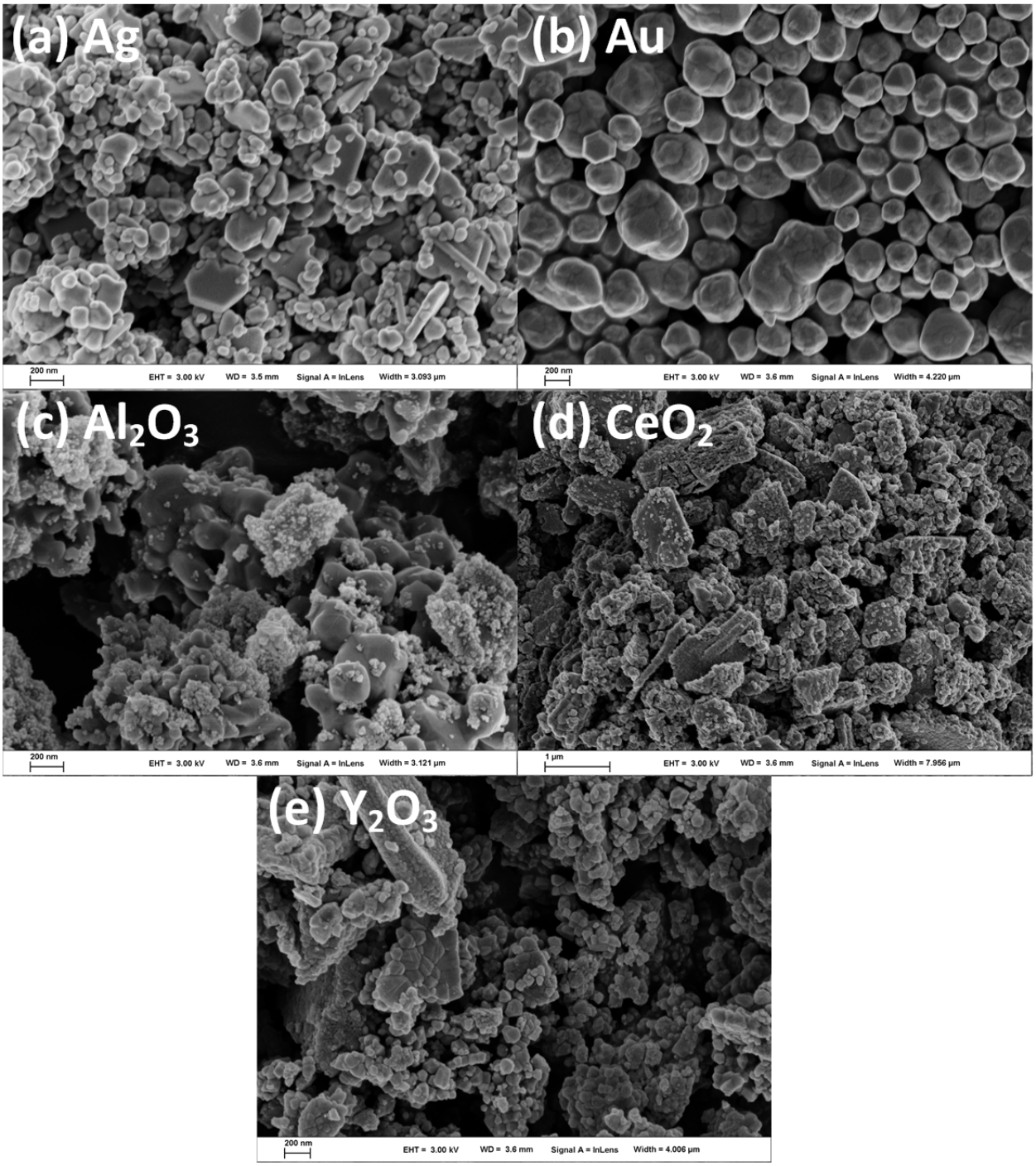

Figure 2. Scanning electron microscope images of (a) silver (Ag), (b) gold (Au), (c) aluminum oxide (Al_2O_3), (d) cerium oxide (CeO_2), and (e) yttrium oxide (Y_2O_3)

3 Results

Figure 3 shows the aerosol concentration (dW) in particles per cm^3 of N_2 as a function of electrical mobility diameter d_p in nanometers. This specific data was generated with Ag aerosol. The median diameter was between 150 and 300 nanometers and agreed well with manufacturer provided data for the particle size distribution. Concentrations below 100 cm^{-3} were not included in data analysis or calculations of aerosol utilization efficiencies due to higher uncertainties.

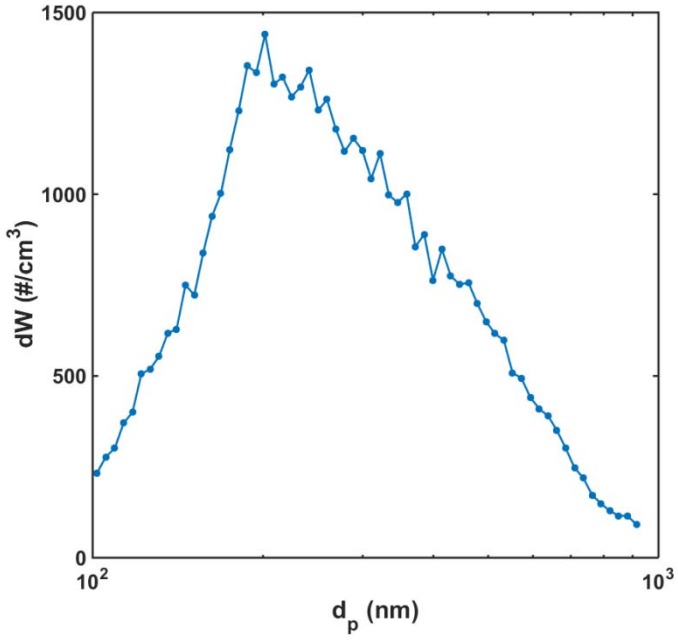

Figure 3. Aerosol particle size distribution measured with electrostatic classifier and condensation particle counter for Ag powder

ICP-MS data are shown in Figure 4. Only data for ^{107}Ag and ^{107}AgO are shown for illustration purposes. ^{109}Ag and ^{107}Ag are naturally occurring isotopes and occur at approximately equal abundances. At time zero the aerosol size began to ramp up in electrical mobility diameter. This was controlled by the electrostatic classifier. The change in analyte intensity (^{107}Ag ions counted per second by the ion detector) is due to two causes: (1) a change in aerosol-gas concentration, and (2) a change in particle diameter. The analyte intensity (counts per second) is denoted as an atom flow rate through the mass spectrometer, $\dot{n}_{ms}$. Without both particle size and gas concentration measurements it would not be possible to calculate the aerosol utilization efficiency from ICP-MS data. Coupling these two experimental capabilities is what makes this data unique. The relative standard deviation in ^{107}Ag data was approximately 10%. ^{107}AgO concentrations were on the order of 0.2-0.5% of the maximum ^{107}Ag concentration. We suspect that these oxide species formed inside the plasma with the trace amount of oxygen inside the argon and nitrogen. The ^{107}AgO intensity was not dependent on time. For the purposes of

calculating aerosol utilization efficiency, values of $\dot{n}_{ms}$ were only used if five times greater than background measurements (taken without aerosol being fed into the plasma).

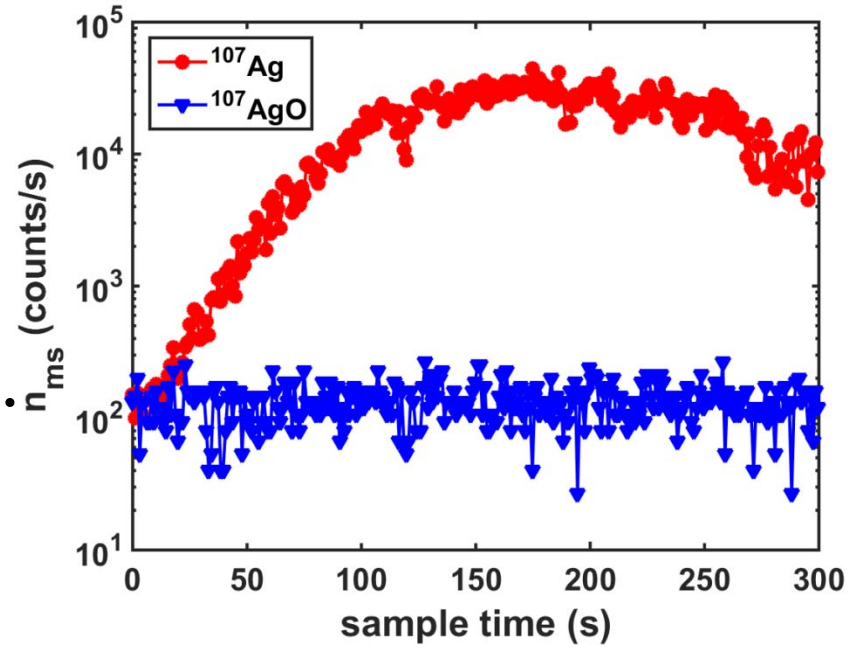

Figure 4. ICP-MS analyte intensity measurement (counts per second) as a function of sample time (particle diameter) for ^{107}Ag and ^{107}AgO

The theoretical number of analyte atoms being fed into the ICP-MS per second was calculated from aerosol-gas concentration data. The aerosol atom flow rate, $\dot{n}_a$, was calculated according to the following equation:

$$\dot{n}_a = dW \cdot \frac{\pi}{6} \rho_m d_p{}^3 \cdot \frac{1}{MW_{compound}} \cdot \frac{mol_{analyte}}{mol_{compound}} \cdot N_A \cdot Q_{N_2} \tag{1}$$

where N_A was Avogadro's number. The aerosol utilization efficiency, E , was then calculated according to the following equation:

$$E = \frac{\dot{n}_{ms}}{\dot{n}_a} \ . \tag{2}$$

The method of Kline and McClintock (1949) was used to calculate uncertainties in calculated values of $\dot{n}_a$ and E. The major uncertainties propagating through the calculation are given below in Table 4.

Table 4. Primary measurement uncertainties propagating through the calculation for aerosol utilization efficiency E

Parameter	Uncertainty (%)
dW	10
Q	10
d_p	20
ρ_m	10
$\dot{n}_{ms}$	10

The uncertainty in $\dot{n}_a$, $U_{\dot{n}_a}$, was calculated as

$$U_{\dot{n}_a} = \left[(0.10)^2 + 9(0.20)^2 + (0.10)^2 + (0.10)^2 \right]^{1/2} = 0.33 . \quad (3)$$

The uncertainty in E, U_E , was calculated as

$$U_E = \left[(0.33)^2 + (0.10)^2 \right]^{1/2} = 0.35 . \quad (4)$$

The uncertainty in E is mostly driven by uncertainties in particle diameter and particle concentration which are used to calculate particle mass injected into the ICP-MS.

Aerosol concentration data in Figure 3 and ICP-MS data in Figure 4 were combined with equations (1) and (2) and plotted in Figure 5. The maximum aerosol utilization efficiency of $2 \cdot 10^{-8}$ occurred around the peak aerosol concentration and median diameter of 250 nm. The aerosol utilization efficiency then dropped by an order of magnitude between 250 nm and 1000 nm. We attribute this loss in aerosol utilization efficiency to incomplete atomization (the breakdown of aerosol particles into atoms inside the plasma) due to particle size. Larger particles were not completely atomized in the plasma due to limited residence times and transient heat and mass transfer rates. Below a certain size, e.g., 250 nm, aerosol utilization efficiency should remain constant if all other factors remain constant and particles are completely atomized. We therefore dismiss the small increase in aerosol utilization efficiency from 100-250 nm as within estimated uncertainty (35%).

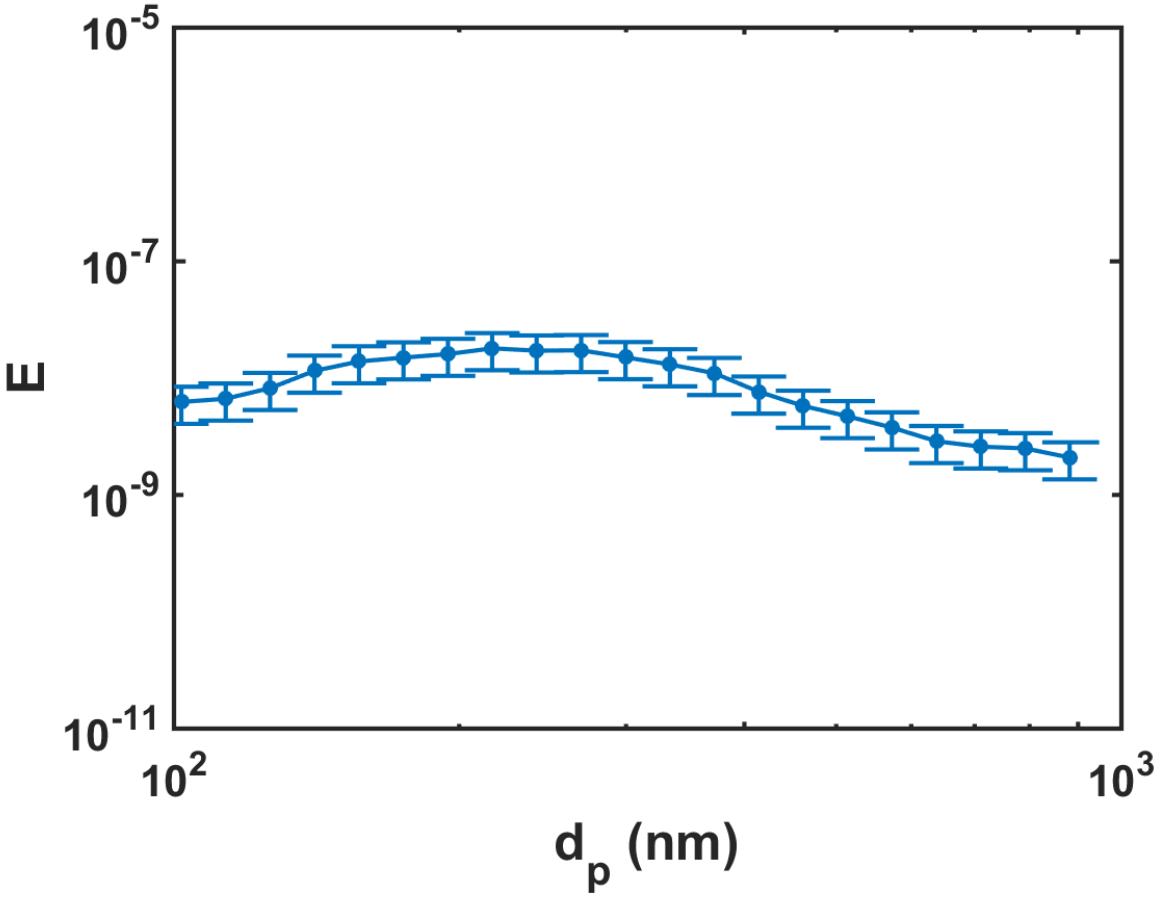

Figure 5. Aerosol utilization efficiency, E, as a function of electrical mobility diameter, d_p for Ag aerosol

The logarithm of aerosol utilization efficiency was plotted against the logarithm of particle size and then fitted with a piecewise function to represent the onset of particle size dependence at a critical particle diameter. We assumed the aerosol utilization efficiency was constant below some critical value of particle diameter. After the critical diameter, we assumed the aerosol utilization efficiency decreased with particle size according to a power law function in agreement with experimental data. The piecewise fitting function was specified as follows:

$$\log_{10}(E) = a \qquad for \qquad \log_{10}(d_p) <= k \tag{5}$$

and,

$$\log_{10}(E) = \frac{a-b}{k}\log_{10}(d_p) + b \qquad for \qquad \log_{10}(d_p) > k\,. \tag{6}$$

The constant k was used to determine the critical diameter, $d_{p,c} = 10^k$. Taking the inverse logarithm of equations (5) and (6) gives the following equations for aerosol utilization efficiency:

$$E = 10^a \qquad for \qquad d_p <= 10^k \tag{7}$$

and,

$$E = 10^b d_p{}^m \qquad for \qquad d_p > 10^k \tag{8}$$

where

$$m = \frac{a-b}{k} \tag{9}$$

Figure 6 through Figure 10 show the logarithm of aerosol utilization efficiency as a function of the logarithm of particle diameter. High and low flow conditions are shown for silver, gold, aluminum oxide, yttrium oxide, and cerium oxide. The low flow condition for cerium oxide was not obtained due to plasma instability for that specific set of experimental parameters. Each experiment was performed in triplicate and all data are shown in the figures.

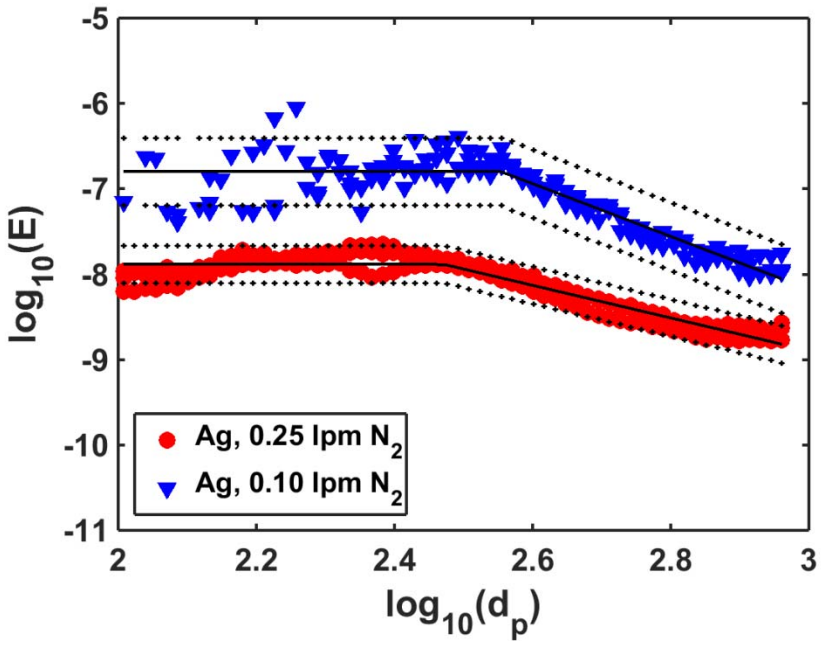

Figure 6. Log_{10}(aerosol utilization efficiency) vs. Log_{10}(particle diameter) for silver aerosol particles

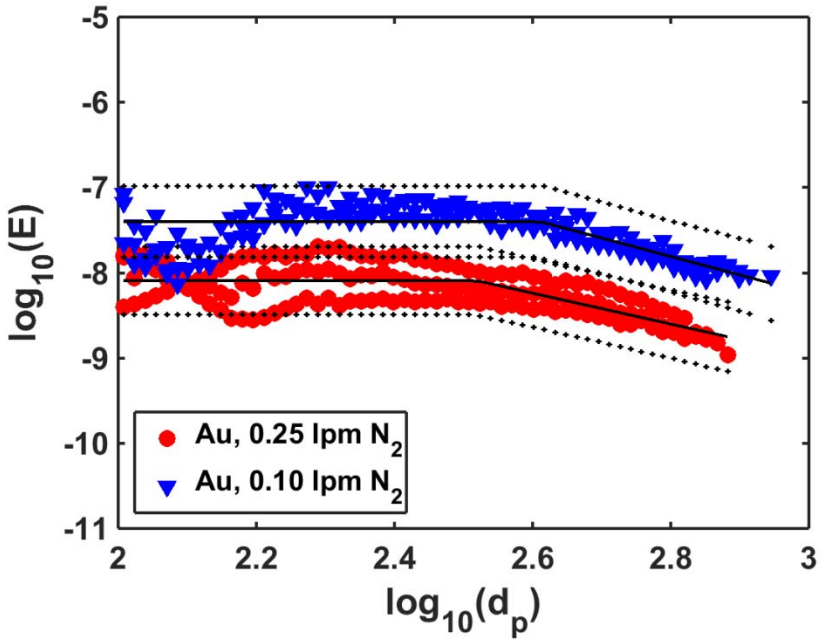

Figure 7. Log_{10}(aerosol utilization efficiency) vs. Log_{10}(particle diameter) for gold aerosol particles

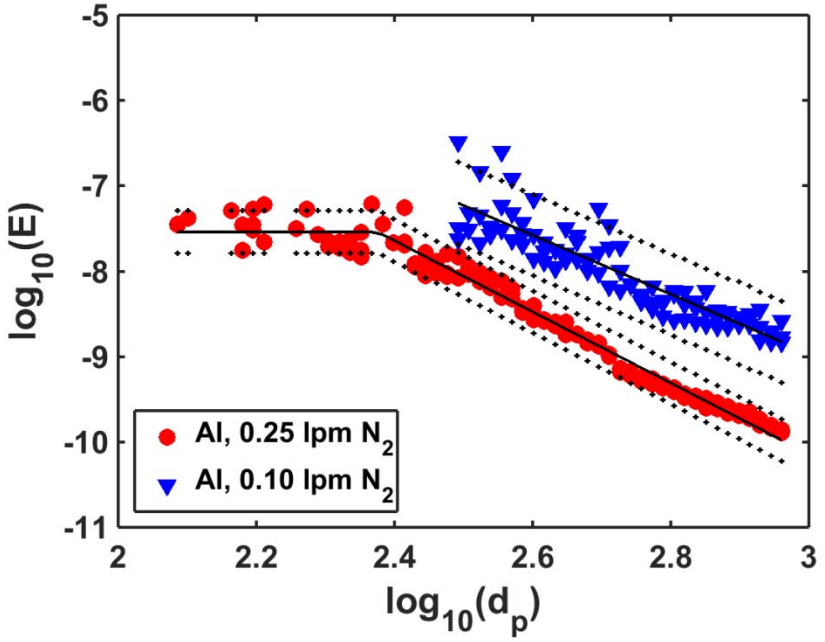

Figure 8. Log_{10}(aerosol utilization efficiency) vs. Log_{10}(particle diameter) for aluminum oxide aerosol particles

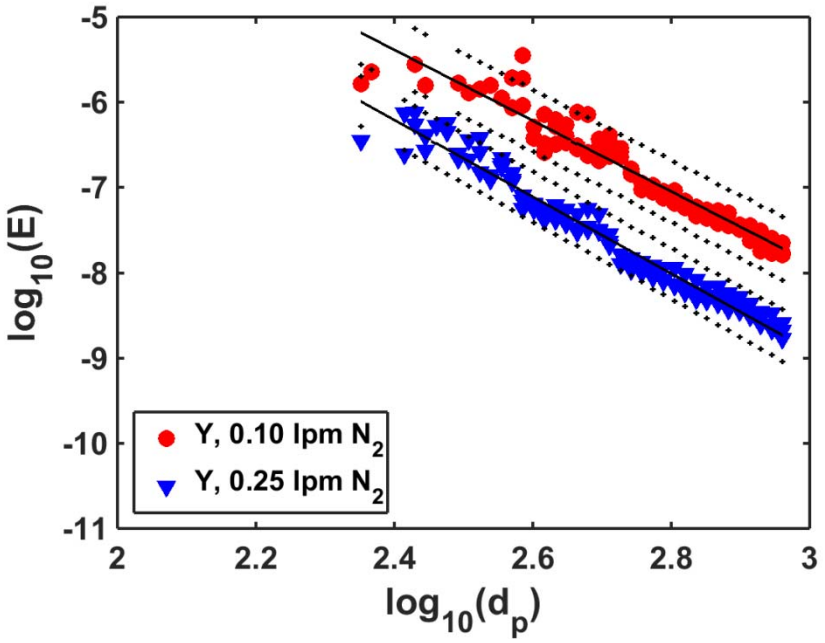

Figure 9. Log_{10}(aerosol utilization efficiency) vs. Log_{10}(particle diameter) for yttrium oxide aerosol particles

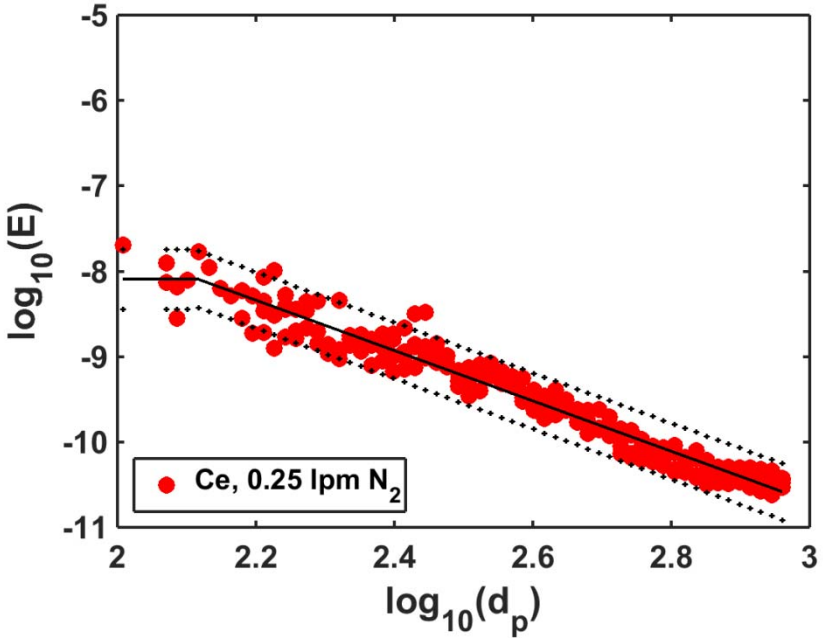

Figure 10. Log_{10}(aerosol utilization efficiency) vs. log(particle diameter) for cerium oxide aerosol particles

Confidence interval bounds on curve fitting parameters were used to calculate the mean critical particle diameter, mean slope, and associated uncertainties. Values are given below in Table 5.

Table 5. Particle composition, nitrogen aerosol generation flow rate (high or low), critical particle diameter ($d_{p,c}$), and slope (m) of the $\log_{10}(E)$ vs. $\log10(d_p)$ curve

Particle Composition	N_2 flow (lpm)	$d_{p,c}$ (nm)	m (-)
Ag	0.1	360 ± 30	-3.1 ± 0.4
Ag	0.25	300 ± 20	-1.9 ± 0.1
Al_2O_3	0.1	-	-3.5 ± 0.3
Al_2O_3	0.25	240 ± 10	-4.2 ± 0.1
Au	0.1	410 ± 50	-2.2 ± 0.7
Au	0.25	330 ± 40	-1.8 ± 0.5
CeO_2	0.25	< 130 ± 20	-2.9 ± -0.1
Y_2O_3	0.1	-	-4.2 ± 0.3
Y_2O_3	0.25	-	-4.5 ± 0.2

Figure 6 and Figure 7 show calculated data for silver and gold, respectively. The more volatile species, silver and gold, had larger critical particle diameters ranging from 300 nm to 500 nm. We attribute larger critical particle diameters to complete particle vaporization occurring for larger particles which delayed the onset of particle size dependent atomization behavior.

Data for Al_2O_3, Y_2O_3, and CeO_2 are shown in Figure 8, Figure 9, and Figure 10, respectively. The oxide species had smaller critical diameters (100 nm to 300 nm). Critical diameters were not observed for all data sets suggesting particle size effects are relevant even below 100 nm for some species. Aerosol concentrations were low for particle diameters less than 300 nm for Al_2O_3 at 0.10 lpm N_2. The same was true for Y_2O_3. Other powders could be used to increase aerosol concentrations at smaller particle sizes and extend the range over which aerosol utilization efficiency can be calculated. The location of the knee in CeO_2 data should be interpreted as $d_{p,c} < 130 \pm 20$ nm. Not enough data is present to conclusively declare there is a transition point at 130 nm.

The magnitude of $m = d\log_{10}(E)/d\log_{10}(d_p)$ reveals differences between volatile and refractory species, and high and low flow conditions (i.e., residence time).

Data for Ag and Au are somewhat inconclusive in this regard. The decreasing portion of the curve should be extended to larger particle sizes (1-5 μm) to more clearly identify the dependence of aerosol utilization efficiency on plasma residence time. Uncertainty in m made it difficult to conclude if there were well defined d_p^{-2} and d_p^{-3} regimes. Some data even suggested that the size dependence was higher than d_p^{-3}, e.g., d_p^{-4}. The effect of particle size on aerosol utilization efficiency for oxidized species Y_2O_3 and Al_2O_3 was more significant ($3 < m < 5$). In addition to particle surface area and volume, heat and mass transfer coefficients may have some dependence on particle diameter leading to power law dependencies stronger than d_p^{-3}.

4 Discussion

4.1 Heat transfer

The ratio of convective and conductive heat transfer rates at the boundary of a particle is given by the Nusselt number,

$$Nu = \frac{h \cdot d_p}{k_g} \ , \tag{10}$$

where h is the convective heat transfer coefficient and k is the thermal conductivity of the surrounding fluid. Re is the particle Reynolds number. The particle Reynolds number gives a ratio of fluid inertial forces to viscous forces:

$$Re = \frac{\rho_g \cdot U_\infty \cdot d_p}{\mu_g} . \tag{11}$$

In (11), ρ_g and μ_g are the gas density and dynamic gas viscosity, respectively. Gas densities and viscosities for argon at high temperature were taken from Carpenter et al. (2012) and Murphy et al. (1994), respectively. For Re << 1, the flow around the particle is considered viscous and Nu = 2. In this limiting case the convective heat transfer coefficient is directly proportional to the thermal conductivity of the fluid and inversely related to particle diameter. As particle diameter approaches the mean free path of the gas, continuum fluid assumptions are no longer valid. There is a transition from continuum to free molecular physics regimes indicated by the dimensionless Knudsen number:

$$Kn = \frac{2\lambda_g}{d_p} \ . \tag{12}$$

In (12), λ_g is the mean free path of gas atoms or molecules. The mean free path was calculated according to the following relationship (McCoy and Cha, 1974):

$$\lambda_g = \frac{\mu_g}{\rho_g}\left(\frac{2k_B T_g}{\pi m_g}\right)^{-0.5}, \tag{13}$$

where the Boltzmann constant is $k_B = 1.381 \cdot 10^{-23}$ J/K, and the gas molecule mass is $m_g = 6.634 \cdot 10^{-26}$ kg for Argon. The average molecular speed is given by

$$\overline{c} = \left(\frac{8k_B T_g}{\pi m_g}\right)^{0.5}. \tag{14}$$

Kennard (1938) derived the heat transfer rate ($\dot{q}$) to a particle in the free molecular regime (subscript *fm*),

$$\dot{q}_{fm} = \alpha\pi\left(\frac{d_p}{2}\right)^2 \frac{P_g \overline{c}}{2}\frac{\gamma+1}{\gamma-1}\left(\frac{T_p}{T_g}-1\right), \tag{15}$$

where the accommodation coefficient, α, is assumed to be on the order of unity, γ is the specific heat capacity ratio taken as a constant independent of temperature, $\gamma = 1.667$ (argon), P_g is gas pressure (1 atm), and T_p is particle temperature. In the continuum regime (subscript *c*) the heat flux to the particle is given by

$$\dot{q}_c = 4\pi\left(\frac{d_p}{2}\right)k_g(T_p - T_g). \tag{16}$$

Fuchs (1959) derived the ratio of actual heat flux to the continuum heat flux as a function of *Kn*, and the free-molecular and continuum heat fluxes:

$$\frac{\dot{q}}{\dot{q}_c} = \left(\frac{1}{1+Kn} + \frac{\dot{q}_c}{\dot{q}_{fm}}\right)^{-1}. \tag{17}$$

Equation (17) is valid over the entire range of *Kn*. A more detailed description of continuum-transition-free-molecular regime heat transfer can be found in the literature for laser induced incandescence of aerosol particles (Liu et al., 2006).

The ratio $\dot{q}/\dot{q}_c$ is plotted against *Kn* in Figure 11. The following values were assumed: T_p = 1,000 K, T_g =10,000 K, and k_g = 0.65 W/mK where the thermal conductivity of argon can be taken from Devoto et al. (1967) for $T_g > 5000$ K and Hoshino et al. (1986) for $T_g < 5000$ K. The crossover from the continuum regime to the transition regime occurs at *Kn*~0.01. The crossover from the transition regime to free molecular regime occurs at *Kn*~10. A broad range of *Kn* is shown in the figure for the purpose of comparison to other works. The slip flow regime studied extensively by Pfender (1985) is valid for $0.001 < Kn < 0.1$ where particles would be in the range of 10-100 μm in particle diameter. Particles injected in this work were much smaller than most particles studied in the works outlined in the *Introduction* section.

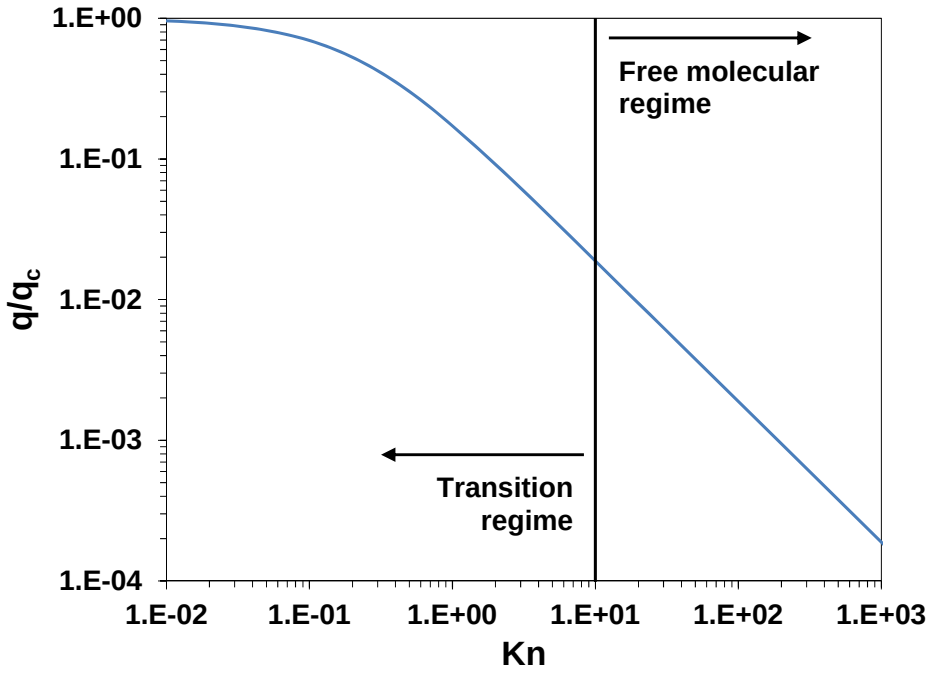

Figure 11. Ratio of actual heat transfer to nanoparticle to heat transfer in the continuum regime as a function of particle Knudsen number. Mean free path of argon was calculated at 10,000K.

The ratio $\dot{q}/\dot{q}_c$ is plotted against d_p in Figure 12. The free-molecular to transition regime crossover occurs at approximately 2 μm. All data collected here were in the free-molecular regime. The heat transfer rate to a 100 μm is approximately 51% of the continuum limit. Not until particle diameter reaches approximately 1000 μm is the heat transfer rate 90% of the continuum limit.

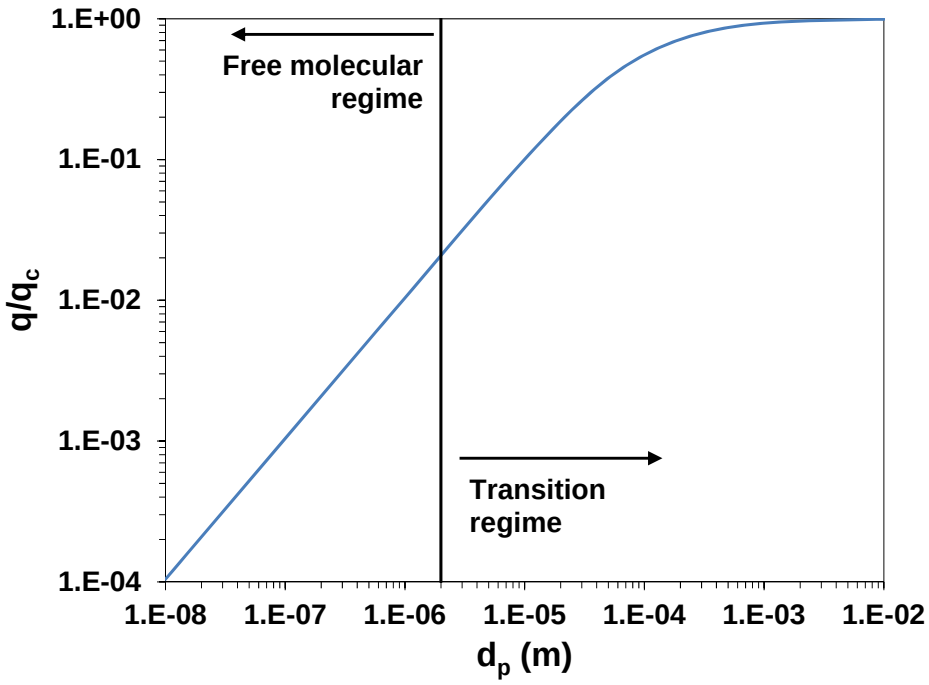

Figure 12. Ratio of actual heat transfer to nanoparticle to heat transfer in the continuum regime as a function of particle diameter. Mean free path of argon was calculated at 10,000K.

4.2 Equilibrium Temperature

The particle Biot number is given by

$$Bi_p = \frac{h_\infty \cdot d_p}{k_p} \tag{18}$$

and gives the ratio of heat transfer resistances at the surface (convection) to the interior conduction resistance. If $Bi_p \le 0.1$, it is generally assumed that the interior of the particle is at uniform temperature. This is often called a lumped capacitance model (Incropera and Dewitt 2002). For the particle materials and gas conditions in this study, $10^{-3} \le Bi_p \le 10^{-2}$. We thus conclude that internal particle temperature gradients do not have a significant effect on particle atomization. This is not always the case (e.g., large particles) and others have accounted for internal temperature gradients in their numerical models of aerosol evaporation (Yao et al. 2009).

The Fourier number gives the ratio of thermal diffusion to thermal storage within the interior of the particle:

$$Fo_p = \frac{\alpha_p t}{d_p^{\,2}}. \tag{19}$$

In (19), the thermal diffusivity is given by $\alpha_p = k_p / \rho_p C_p$ where C_p is the thermal heat capacity of the particle. For equation (19), we will use the characteristic time of 20 milliseconds which is the approximate bulk torch velocity (~ 1.3 m/s) normalized by the length of torch in which particle atomization occurs (~ 0.0254 m). For the particle materials and gas conditions in this study, $10^4 \le Fo_p \le 10^6$. We thereby conclude that the time over which particle atomization occurs is long with respect to the thermal equilibration time of the particle; particle temperature is not assumed to be transient but rather assumed to reach its equilibrium temperature very quickly.

Under steady-state, equilibrium, evaporative conditions, the heat transfer to the particle is balanced by the energy carried away from the particle by mass transfer, $\dot{m}_{evap}$, and phase change:

$$\dot{q}_c = \dot{m}_{evap} \cdot h_{fg}\ , \tag{20}$$

where h_{fg} is the enthalpy of vaporization. Theoretical heat transfer rates for Au and Ag particles were calculated according to the methods outlined in section *4.1. Heat transfer*. Only Au and Ag were considered here due to the complexity of calculating enthalpy of phase change, and the sparsity of vapor pressure data, for oxidized species. Vapor pressure data for Au and Ag are also readily available (CRC 1999). Our analysis indicates that the particle temperature would need to exceed the boiling point of these materials for the heat transfer rate to be balanced by mass transfer and associated phase change. This is different from other ICP-MS sample injection techniques where dissolved analyte atoms are injected in the form of dilute aqueous droplets. The heat of vaporization of water is relatively large thereby reducing the droplet temperature below the boiling point of water (Benson, 2001); water droplets in ICP-MS evaporate rather than boil.

4.3 Evaporation

In addition to the simple equilibrium condition assumed in (20), evaporative behavior can be modeled by the kinetic theory of gases. The particle diameter at arbitrary time t is given by the following:

$$d_p(t) - d_{p0} = -\frac{1}{4}\frac{c_i M_i P_v}{RT} t\ , \tag{21}$$

where P_v is the vapor pressure at the surface of the particle. The aerosol utilization efficiency, the fraction of particle atomized, is then given by

$$E = 1 - \left(\frac{d_{pf}}{d_{p0}} \right)^3 = 1 - \left[1 - \frac{1}{4} \frac{c_i M_i P_v \tau}{RT} \frac{1}{d_{p0}} \right]^3 . \tag{22}$$

We then define a parameter,

$$a = \frac{1}{4} \frac{c_i M_i P_v \tau}{RT} , \tag{23}$$

such that (22) can be written more succinctly and utilized for data fitting operations,

$$E = 1 - \left(1 - \frac{a}{d_{p0}} \right)^3 , \tag{24}$$

where only initial particle diameter is known *a priori*. Au and Ag data were fitted with (24) and replotted in Figure 13 and Figure 14, respectively. From equation (22) and (24), one can see that $0 \le 1 - a / d_{p0} \le 1$ due to limitations on d_{pf} / d_{p0}. In this range of values the size dependence of E varies from $d_p^{\,0}$ to $d_p^{\,-1}$. The solid lines represent curve fits of the form of equation (6). The dashed lines represent curve fits of the form of equation (24). As can be seen in the figure, evaporative phenomena do not predict the functionality (e.g., $E \sim dp^{-3}$) observed in experimental data. Once again we observe data trends that suggest purely evaporative phenomena are not sufficient to describe the process of nano-particulate aerosol atomization in an inductively coupled plasma.

Additionally, under evaporative conditions, the dependence of aerosol utilization efficiency on particle size varies, thus, disparities in slope presented in Table 5 would be expected depending on the dimensionless parameter a / d_{p0}; m at the low and high flow conditions for silver should not be necessarily be equal due to the shift in a / d_{p0}. We hypothesize that boiling does occur and that self-similar behavior could exist for boiling as well as evaporation.

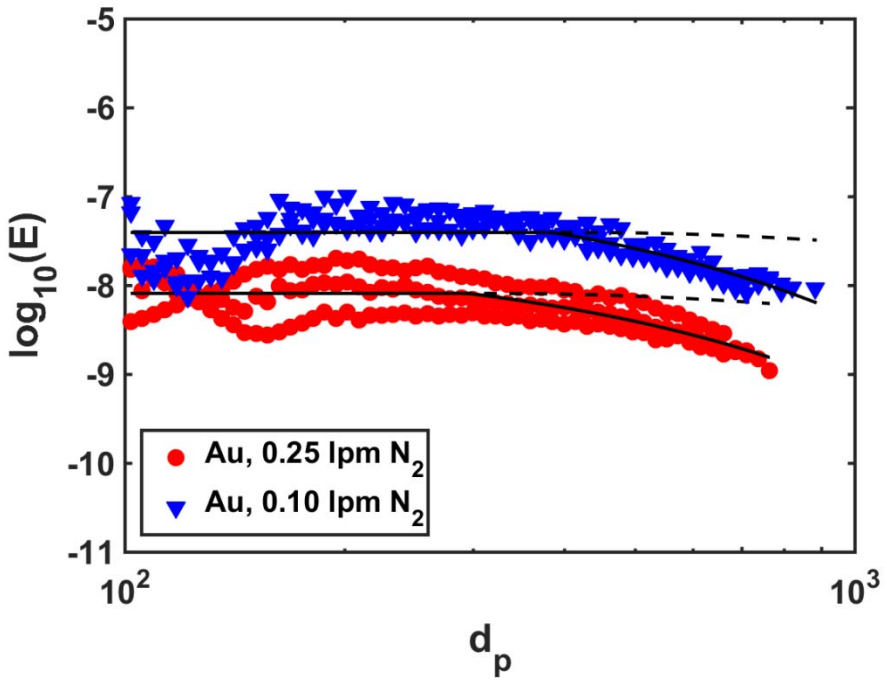

Figure 13. Log_{10}(aerosol utilization efficiency) vs. particle diameter for Au aerosol including power law curve fit, equation (6), and evaporative theory curve fit, equation (24)

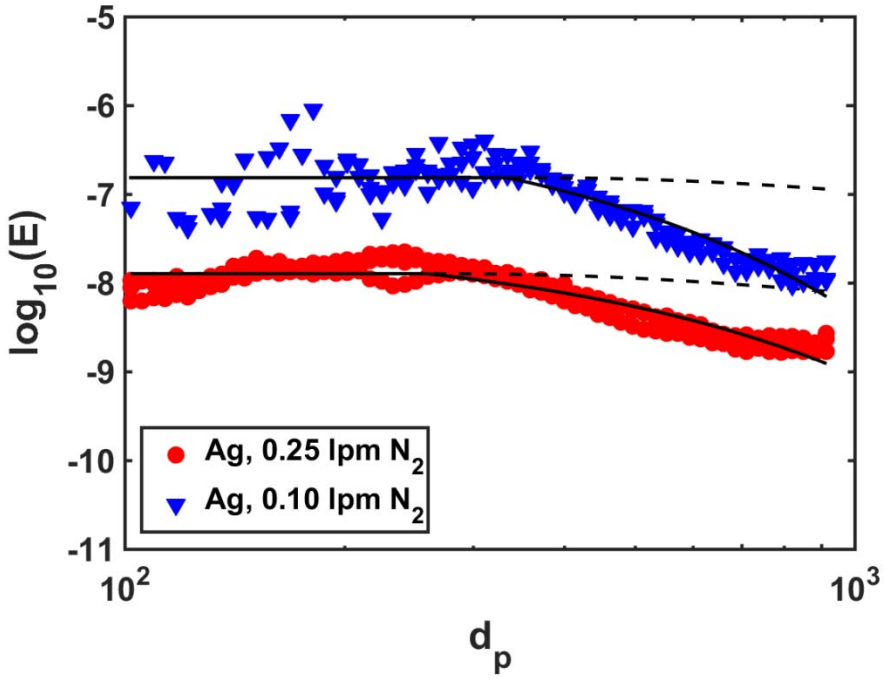

Figure 14. Log_{10}(aerosol utilization efficiency) vs. particle diameter for Ag aerosol including power law curve fit, equation (6), and evaporative theory curve fit, equation (24)

We hypothesize that boiling phenomena may augment evaporative behavior adding a mass transfer mechanism that is volumetrically dependent rather than solely surface dependent. Rapid particle boiling may result in particle fragmentation which could act to disperse material away from the torch centerline and remove it from the stream sampled by the skimmer cone. More work is needed to analyze boiling behavior and the behavior of oxide species. Vapor pressure and enthalpy data are available in Ackermann et al. (1958), Brewer et al. (1952), Touloukian et al. (1966), JANAF Tables (Chase 1998) for aluminum species, and Pankratz and Mrazek (1982).

5 Conclusions

Aerosols of known particle size, composition, and gas concentration were generated and injected directly into an inductively coupled plasma mass spectrometer (ICP-MS). To do so, polydisperse aerosols were generated and size segregated in an electrostatic classifier providing size control between 100 nm and 1000 nm. After size segregation, particles were either counted in a condensation nuclei counter or injected into an ICP-MS. An aerosol utilization efficiency for the ICP-MS was calculated using the calculated atomic injection rate (aerosol particles in) and atomic count rate of the ICP-MS (atoms detected). Torch residence time, particle size, and particle composition were observed to affect the aerosol utilization efficiency. The aerosol utilization efficiencies of gold and silver were relatively constant up to approximately 300 nm to 400 nm in size after which the utilization efficiency decreased with increasing particle size. The particle size dependence varied with residence time and particle composition. Empirical data suggested that aerosol utilization efficiencies varied as d_p^{-2} *to* d_p^{-4}. Data might suggest that the dependence on particle size is stronger for refractory species and weaker for volatile species but experimental uncertainties need to be reduced to support definitive statements. Free-molecular heat and mass transfer theory for evaporation was applied to experimental data but did not adequately predict the particle size dependence observed in aerosol utilization efficiencies. Data suggests that particle temperatures are elevated above the boiling point temperature and boiling phenomena augment aerosol utilization in ICP. Rapid particle boiling may result in particle fragmentation leading to material being dispersed away from the torch centerline. More work is needed to model the behavior of metal-oxides due to challenges in calculating enthalpy of phase change and sparse vapor pressure data.

References

Chapman and Hall/CRCnetBASE. (1999). CRC handbook of chemistry and physics, Boca Raton, FL.

Ackermann, R. J., and Thorn, R.J. (1961). Vaporization of Oxides. Progress in Ceramic Sciences 1:39-88.

Benson, C. M., Gimelshein, S. F., Levin, D. A., Montaser, A. (2001). Simulation of droplet heating and desolvation in an inductively coupled plasma - Part I. Spectrochim Acta B 56:1097-1112.

Bernardi, D., Colombo, V., Ghedini, E., Mentrelli, A., Trombetti, T. (2004). 3-D numerical simulation of fully-coupled particle heating in ICPTs. Eur Phys J D 28:423-433.

Brewer, L. (1953). The Thermodynamic Properties of the Oxides and Their Vaporization Processes. Chem Rev 52:1-75.

Carpenter, J. H., Root, S., Cochrane, K.R., Flicker, D.G., and T.R. Mattson (2012). Equation of state of argon: experiments on Z, density functional theory (DFT) simulations, and wide-range model, Albuquerque, NM, 1-54.

Chase, M. W. and National Institute of Standards and Technology (U.S.) (1998). NIST-JANAF thermochemical tables. American Chemical Society; American Institute of Physics for the National Institute of Standards and Technology, Washington, DC.

Chen, X., and E. Pfender (1982). Heat Transfer to a Single Particle Exposed to a Thermal Plasma. Plasma Chem Plasma P 2:185-212.

Chen, X., and E. Pfender (1982). Unsteady Heating Radiation Effects of Small Particles in a Thermal Plasma. Plasma Chem Plasma P 2:293-316.

Chen, X., and E. Pfender (1983). Effect of the Knudsen Number on Heat Transfer to a Particle Immersed into a Thermal Plasma. Plasma Chem Plasma P 3:17.

Chen, X., and E. Pfender (1983). Behavior of Small Particles in a Thermal Plasma Flow. Plasma Chem Plasma P 3:351-366.

Chen, X. (1988). Particle Heating in a Thermal Plasma. Pure Appl Chem 60:651-662.

Cheng, Y. S., Yeh, H. C., Allen, M. D. (1988). Dynamic Shape Factor of a Plate-Like Particle. Aerosol Sci Tech 8:109-123.

DeCarlo, P. F., Slowik, J. G., Worsnop, D. R., Davidovits, P., Jimenez, J. L. (2004). Particle morphology and density characterization by combined mobility and aerodynamic diameter measurements. Part 1: Theory. Aerosol Sci Tech 38:1185-1205.

Devoto, R. S. (1967). Transport Coefficients of Partially Ionized Argon. Phys Fluids 10:354-364.

Flagan, R. C. (2008). Differential Mobility Analysis of Aerosols: A Tutorial. Kona Powder Part J 26:254-268.

Flamigni, L., Koch, J., Gunther, D. (2012). Experimental and theoretical investigations about the vaporization of laser-produced aerosols and individual particles inside inductively-coupled plasmas - Implications for the extraction efficiency of ions prior to mass spectrometry. Spectrochim Acta B 76:70-76.

Fuks, N. A. (1959). Evaporation and droplet growth in gaseous media. Pergamon Press, London.

Glaus, R., Kaegi, R., Krumeich, F., Gunther, D. (2010). Phenomenological studies on structure and elemental composition of nanosecond and femtosecond laser-generated aerosols with implications on laser ablation inductively coupled plasma mass spectrometry. Spectrochim Acta B 65:812-822.

Gonzalez, J. J., Liu, C., Wen, S. B., Mao, X., Russo, R. E. (2007). Glass particles produced by laser ablation for ICP-MS measurements. Talanta 73:577-582.

Gonzalez, J. J., Liu, C. Y., Wen, S. B., Mao, X. L., Russo, R. E. (2007). Metal particles produced by laser ablation for ICP-MS measurements. Talanta 73:567-576.

Hanselman, D. S., Sesi, N. N., Huang, M., Hieftje, G. M. (1994). The Effect of Sample Matrix on Electron-Density, Electron-Temperature and Gas Temperature in the Argon Inductively-Coupled Plasma Examined by Thomson and Rayleigh-Scattering. Spectrochim Acta B 49:495-526.

Hoshino, T., Mito, K., Nagashima, A., Miyata, M. (1986). Determination of the Thermal-Conductivity of Argon and Nitrogen over a Wide Temperature-Range through Data Evaluation and Shock-Tube Experiments. Int J Thermophys 7:647-662.

Incropera, F. P. and DeWitt, D. P. (2002). Fundamentals of heat and mass transfer. J. Wiley, New York.

Kennard, E. H. (1938). Kinetic theory of gases, with an introduction to statistical mechanics. McGraw-Hill Book Company, inc., New York, London.

Kline, S. J., and McClintock, F. A. (1953). Describing Uncertainties in Single-Sample Experiments. Mech. Eng., 75 (1):3–8.

Koch, J., Heiroth, S., Lippert, T., Gunther, D. (2010). Femtosecond laser ablation: Visualization of the aerosol formation process by light scattering and shadowgraphic imaging. Spectrochim Acta B 65:943-949.

Kovacs, R., Nishiguchi, K., Utani, K., Gunther, D. (2010). Development of direct atmospheric sampling for laser ablation-inductively coupled plasma-mass spectrometry. J Anal Atom Spectrom 25:142-147.

Lee, S. Y., Widiyastuti, W., Tajima, N., Iskandar, F., Okuyama, K. (2009). Measurement of the Effective Density of Both Spherical Aggregated and Ordered Porous Aerosol Particles Using Mobility- and Mass-Analyzers. Aerosol Sci Tech 43:136-144.

Lee, Y. C., Chyou, Y. P., Pfender, E. (1985). Particle Dynamics and Particle Heat and Mass-Transfer in Thermal Plasmas .2. Particle Heat and Mass-Transfer in Thermal Plasmas. Plasma Chem Plasma P 5:391-414.

Lee, Y. C. and Pfender, E. (1987). Particle Dynamics and Particle Heat and Mass-Transfer in Thermal Plasmas .3. Thermal Plasma-Jet Reactors and Multiparticle Injection. Plasma Chem Plasma P 7:1-27.

Lindner, H. and Bogaerts, A. (2011). Multi-element model for the simulation of inductively coupled plasmas: Effects of helium addition to the central gas stream. Spectrochim Acta B 66:421-431.

Liu, F., Daun, K. J., Snelling, D. R., Smallwood, G. J. (2006). Heat conduction from a spherical nano-particle: status of modeling heat conduction in laser-induced incandescence. Appl Phys B-Lasers O 83:355-382.

McCoy, B. J., and C.Y. Cha (1974). Transport Phenomena in the Rarefied Gas Transition Regime. Chemical Engineering Science 29:381-388.

McMurry, P. H., Wang, X., Park, K., Ehara, K. (2002). The relationship between mass and mobility for atmospheric particles: A new technique for measuring particle density. Aerosol Sci Tech 36:227-238.

Murphy, A. B. and Arundell, C. J. (1994). Transport-Coefficients of Argon, Nitrogen, Oxygen, Argon-Nitrogen, and Argon-Oxygen Plasmas. Plasma Chem Plasma P 14:451-490.

Myojo, T., Takaya, M., Ono-Ogasawara, M. (2002). DMA as a gas converter from aerosol to "Argonsol" for real-time chemical analysis using ICP-MS. Aerosol Sci Tech 36:76-83.

Nishiguchi, K., Utani, K., Fujimori, E. (2008). Real-time multielement monitoring of airborne particulate matter using ICP-MS instrument equipped with gas converter apparatus. J Anal Atom Spectrom 23:1125-1129.

Okada, Y., Yabumoto, J., Takeuchi, K. (2002). Aerosol spectrometer for size and composition analysis of nanoparticles. J Aerosol Sci 33:961-965.

Pankratz, L. B. and Mrazek, R. V. (1982). Thermodynamic properties of elements and oxides. U.S. Dept. of the Interior For sale by U.S. G.P.O., Washington, D.C.

Pfender, E. (1985). Heat and Momentum-Transfer to Particles in Thermal Plasma Flows. Pure Appl Chem 57:1179-1195.

Pfender, E. and Lee, Y. C. (1985). Particle Dynamics and Particle Heat and Mass-Transfer in Thermal Plasmas .1. The Motion of a Single-Particle without Thermal Effects. Plasma Chem Plasma P 5:211-237.

Punjabi, S. B., Sahasrabudhe, S. N., Ghorui, S., Das, A. K., Joshi, N. K., Kothari, D. C., Ganguli, A. A., Joshi, J. B. (2014). Flow and Temperature Patterns in an Inductively Coupled Plasma Reactor: Experimental Measurements and CFD Simulations. Aiche J 60:3647-3664.

Purdue University. Thermophysical Properties Research Center., Touloukian, Y. S., Air Force Materials Laboratory (U.S.) (1967). Thermophysical properties of high temperature solid materials. Macmillan, New York,.

Tendero, C., Tixier, C., Tristant, P., Desmaison, J., Leprince, P. (2006). Atmospheric pressure plasmas: A review. Spectrochim Acta B 61:2-30.

Walle, M., Koch, J., Flamigni, L., Heiroth, S., Lippert, T., Hartung, W., Gunther, D. (2009). Detection efficiencies in nano- and femtosecond laser ablation inductively coupled plasma mass spectrometry. Spectrochim Acta B 64:109-112.

Yang, P. Y., Horner, J. A., Sesi, N. N., Hieftje, G. M. (2000). Comparison of simulated and experimental fundamental ICP parameters. Spectrochim Acta B 55:1833-1845.

Yao, Y. C., Hossain, M., Watanabe, T. (2009). Numerical and Experimental Investigation on the In-Flight Melting Behaviour of Granulated Powders in Induction Thermal Plasmas. Plasma Sci Technol 11:71-77.

Young, R. M. and Pfender, E. (1985). Generation and Behavior of Fine Particles in Thermal Plasmas - a Review. Plasma Chem Plasma P 5:1-37.

Young, R. M. and Pfender, E. (1987). Nusselt Number Correlations for Heat-Transfer to Small Spheres in Thermal Plasma Flows. Plasma Chem Plasma P 7:211-229.